International Journal of Minerals, Metallurgy and Materials
Volume 24, Number 5, May 2017, Page 550
DOI: 10.1007/s12613-017-1436-z

Effect of coaxial laser cladding parameters on bead formation

A.I. Noskov, A.Kh. Gilmutdinov, and R.M. Yanbaev

Kazan National Research Technical University, 10 Karl Marx Str., Kazan 420111, Republic of Tatarstan, Russian Federation

(Received: 10 October 2016; revised: 28 November 2016; accepted: 29 November 2016)

Abstract: We investigated the shape and morphology of nickel-based powder particles (Sulzer Metco) and coatings produced by laser gas–powder deposition onto steel substrates. Laser deposition was performed using an LC-10 IPG-Photonics laser complex equipped with a 10-kW fiber laser. The shape and microstructure of the samples were studied using optical and electronic microscopy and X-ray diffraction analysis. The results showed that the deposition speed and laser power significantly influenced the shape and size of the beads. The depth of diffusion of nickel into the steel substrate after deposition was less than 20 μm; the microstructure of the resulting coating was fcc Fe_3Ni. As a result, detailed information about the form and shape of the filler powder, modes of its deposition, and the resulting coating structure was obtained; this information is important for the production of high-quality products by additive technologies.

Keywords: laser cladding; additive manufacturing; microstructure; morphology; bead formation

1. Introduction

Laser deposition is a modern technology for producing high-quality coatings [1–3]. In this technique, laser radiation heats (or partially melts) the substrate while filler powder, transported by a gas jet, is injected into the heating spot [4–5]. The gas–powder jet can be supplied either laterally relative to the laser beam or symmetrically from all sides, shrinking into the focus cone (coaxial cladding) [6]. Mixing of the filler product with the base material occurs when the laser power, moving velocity of the laser spot, and the feed rate of the powder are appropriately chosen.

Obtaining high-quality products by the laser deposition technique requires a series of test experiments to establish optimal operational modes. As each experimental unit has its own characteristics, no general parameters exist for achieving optimal quality. In addition, the properties of the produced coating mainly depend on the properties of the filler material [7–8]. Therefore, analyses of the shape and morphology of powder particles are also necessary to achieve a high-quality coating. Coatings created from a suitable powder in the regime of optimal deposition modes have significantly higher durability than those created from mono-materials [9].

Thus, establishing optimal deposition parameters and analyzing the filler material and resulting coatings are essential for conducting experiments to investigate the influences of the fractional composition, the shape of powder particles, and other factors on laser gas–powder deposition.

2. Experimental

Laser deposition was performed using an LC-10 IPG-Photonics laser complex equipped with a 10-kW fiber laser with a radiation wavelength of 1064 nm and a KUKA KR 120 R 2700 extra HA industrial robot [10–13]. The metal powder was injected into the focused laser beam. The powder and the surface of the substrate were melted by the laser, forming a molten pool. The bead was formed by moving the laser focal spot along the substrate. The deposition process was protected by shielding argon delivered through the coaxial nozzle. The shielding gas flow rate was 17 $L \cdot min^{-1}$. Samples were mounted, polished, and etched using standard metallographic techniques for nickel-based superalloys.

A Rigaku SmartLab multipurpose X-ray diffractometer (Cu anode; tube voltage: 45 kV; tube current: 100–200 mA) operated in classical Bragg–Brentano geometry was used for

Corresponding author: A.I. Noskov E-mail: aleks622@yandex.ru

structural analysis of the samples. The scans were performed over the 2θ interval of 10°–110° with a step of 0.03° and a dwell time of 3 s for each step. The powder sample was also rotated around its normal plane at $1000° \cdot min^{-1}$ during the analysis. The microstructure of the powders and microsections were studied using an Auriga CrossBeam workstation (Carl Zeiss) equipped with an INCA X-Max SDD detector for energy-dispersive X-ray microanalysis. An Axio Imager light microscope (Carl Zeiss) was used for visual observation of the samples. The software package Minitab (ver. 16) was used for particle diameter measurements. The fractional composition of the powder was studied using a Malvern Mastersizer 3000, which was equipped with a special module for automatic feeding and sample dispergation (Hydro S). The coating hardness was measured on a Wolpert UH930 universal hardness tester. The hardness measurements were conducted in accordance with standard ISO 6506.A Haver & Boecker sifting device with a set of test sieves with par values of 80 and 112 μm was used to separate the powder fractions.

3. Results and discussion

3.1. Study of the original filler material

Fig. 1 shows the scanning electron microscopy (SEM) images of the filler material particles of the Sulzer Metco powder. Most of the particles have a regular spherical shape, and no agglomeration of the particles is observed.

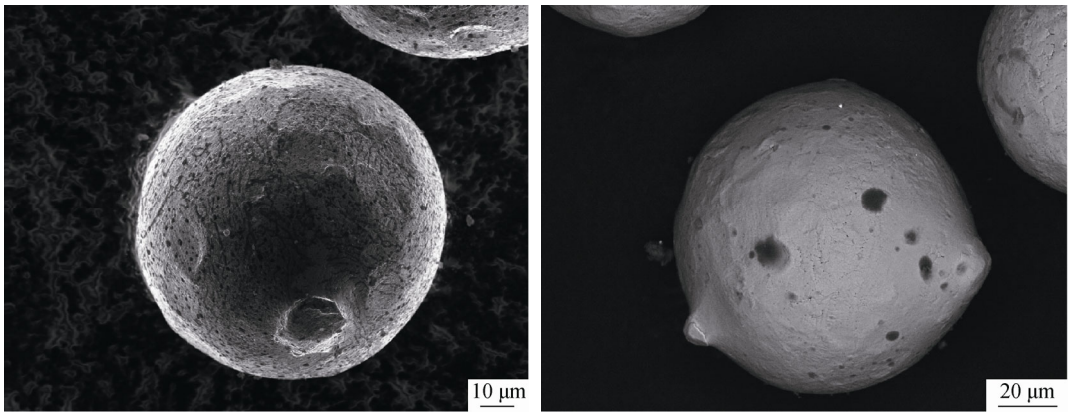

Fig. 1. SEM image of a particle of the filler material (secondary electron imaging mode).

Most of the powder particles have this form, as evident from the powder's electron microscopic images collected in the backscattered electron imaging mode (Fig. 2). The particle size distributions obtained by two independent methods are shown in Fig. 3.

According to the aforementioned results, most of the powder particles can be reasonably assumed to have a uniform spherical shape and size, with an average size of (97 ± 13) μm. Three fractions (65, 95, and 130 μm) from the original powder were prepared to analyze the effect of the fractional composition of the powder on the quality of rolls. The content of the alloying elements (Cr, Fe, and Si) in the nickel base was determined by energy-dispersive X-ray microanalysis of the filler powder (see Table 1).

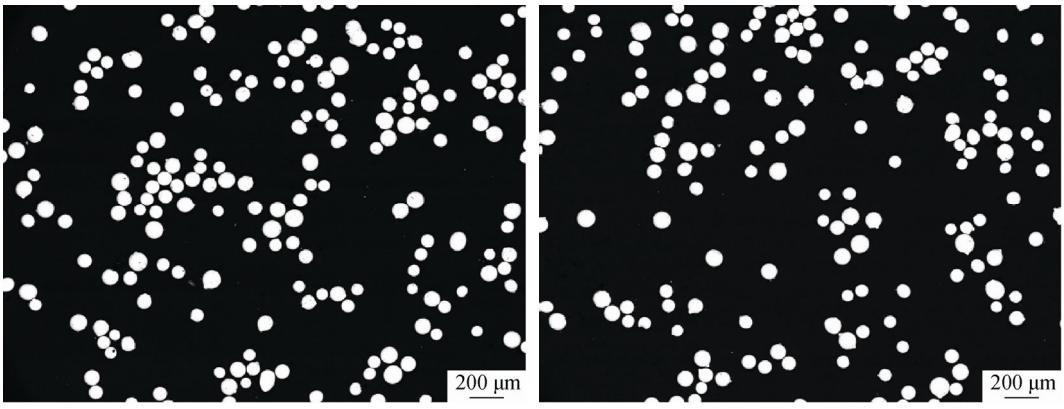

Fig. 2. SEM image of the particles (backscattered electron imaging mode).

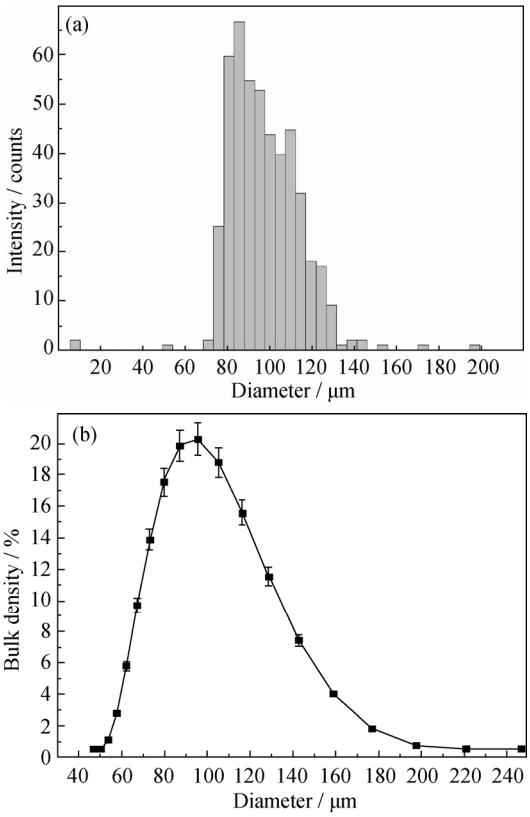

Fig. 3. Histogram of the particle size distribution determined using imaging particle analysis (a) and plot of the particle sizes determined using laser diffraction analysis (b).

Table 1. Chemical composition of the filler powder wt%

Cr	Fe	Si	Al
6.7	1.8	4.7	1.2

3.2. Investigation of the influence of laser deposition parameters on the bead shape

A series of test experiments were conducted to determine the optimal parameters for laser deposition of nickel powder onto a steel substrate. The objective of the test experiments was to determine the dependence of the shape of the deposited bead on the laser power, the speed of laser spot movement, and the powder granulometric composition. A series of single beads were thus obtained. The shape of the beads and the coefficient of mixing were analyzed. Other authors have conducted similar experiments with iron-based powder to select coaxial cladding modes [14]. Devoyno *et al.* [7] investigated the beads obtained by laser cladding with nickel-based self-fluxing alloy. Our results are in good agreement with the results of these previous studies.

The height H, width L, depth h of the substrate melt, deposited layer area S_c, and area of the remelting base metal S_m (see Fig. 4) were defined for analyzing the form of the deposited bead. The mixing ratio (D) and the bead form (K) were evaluated as follows:

$$D = \frac{S_m}{S_m + S_c} \quad (1)$$

$$K = \frac{H}{L} \quad (2)$$

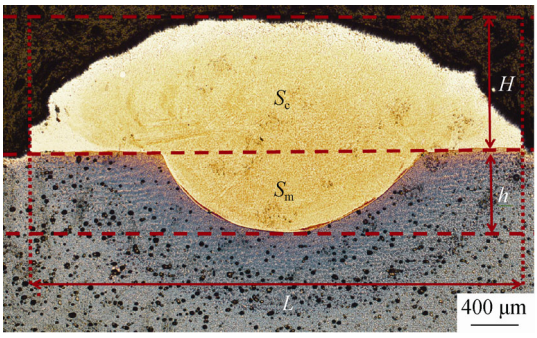

Fig. 4. Cross-section of the bead deposited with laser power P = 3.3 kW, deposition speed V = 15 mm·s^{-1}, and powder flow rate F = 39 g·min^{-1}.

The results revealed that the optimum value of the laser power P is (3 ± 0.3) kW. At a given radiation power, the resulting bead has a symmetrical shape and a small mixing ratio (Fig. 5).

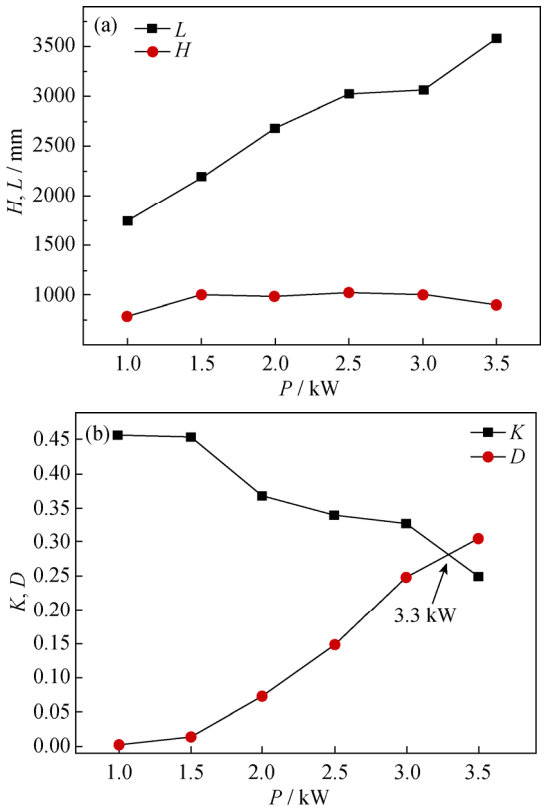

Fig. 5. Dependence of bead length and height on the laser power (a) and dependence of mixing ratio and bead form on the laser power (b).

By analyzing the influence of the deposition speed on the bead form, we established that the mixing ratio and optimal bead forms were achieved at a speed of 15 mm·s^{-1} (Fig. 6).

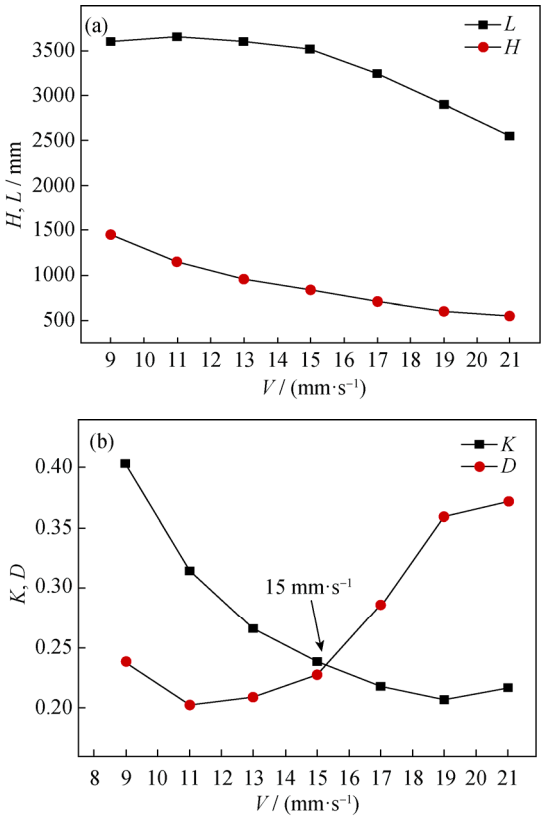

Fig. 6. Dependence of bead height and length on the deposition rate (a) and dependence of the mixing ratio and bead form on the deposition rate (b).

Notably, no experiments have been conducted on the effect of powder flow on the shape of beads. In all the experiments, the powder flow rate was 39 g·min^{-1}. This value was experimentally determined beforehand and accepted as optimal.

Our study on the influence of the powder fractional composition on the bead shape revealed that the size of powder particles directly affects the roughness of the resulting products. A substantial change in the shape of beads was not detected. In addition, our results are in good agreement with those of Kong *et al.* [14], who examined the effect of powder particle size on the efficiency of the deposition process, the porosity of the resulting products, and the quality of the resulting parts in detail.

3.3. Study of the obtained coating

The type, shape, and geometric dimensions of the sample and the resulting bead are shown in Fig. 4. The width of the bead is 3.5 mm, the height is 0.8 mm, and depth-of-penetration is 0.6 mm.

As evident from Fig. 7, the surface layer of the substrate has a martensitic structure. Analysis of the substrate structure shows that the ferrite–pearlite structure formed in the vicinity of the deposition zone under the influence of high-speed heating and subsequent cooling changed into fine-needle martensite. Martensitic needles formed closer to the melting zone and were enriched with the elements of the deposited powder.

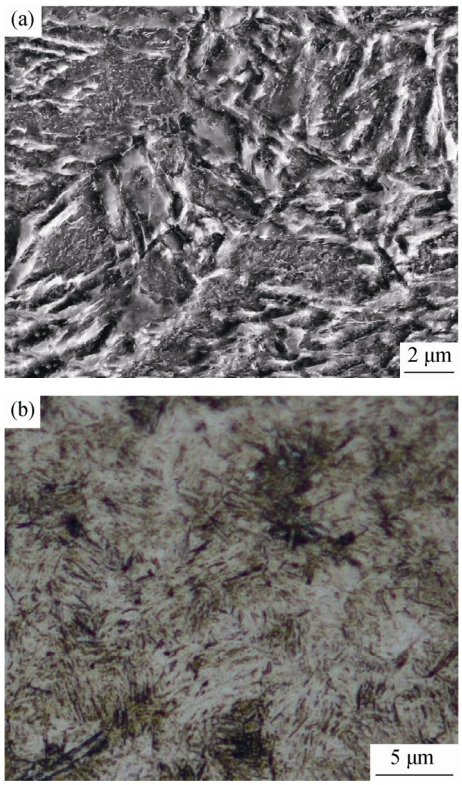

Fig. 7. Electron microscopy image of the initial substrate (a) and optical image of the substrate after deposition (b).

A well-developed dendritic structure is observed in the microstructure of the deposited nickel powder. The dendritic axes' orientation toward the thermal center from the surface of the substrate (Fig. 8) shows the melting of the filler powder during laser deposition. Low porosity is established in the deposited layer of nickel powder.

A layer that comprises cells enriched with nickel exists directly on the border of the Ni layer/substrate (Fig. 9). As soon as the temperature gradient decreases, the cells convert into dendrites.

Energy-dispersive X-ray microanalysis of the deposited metal revealed no burning out of alloying elements during deposition. In the fusion zone, mixing of the primary and deposition metals is minimal. The presence of traces of the base metal (Fe) is observed only in a small area (<20 μm) along the line of fusion (Fig. 10).

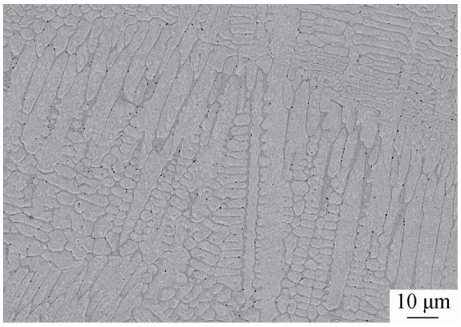

Fig. 8. Electron microscopic image of the nickel layer.

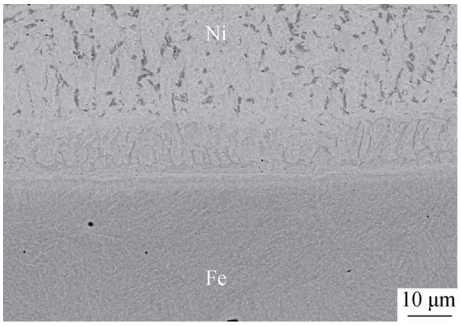

Fig. 9. Electron microscopic image of the nickel/substrate transition layer.

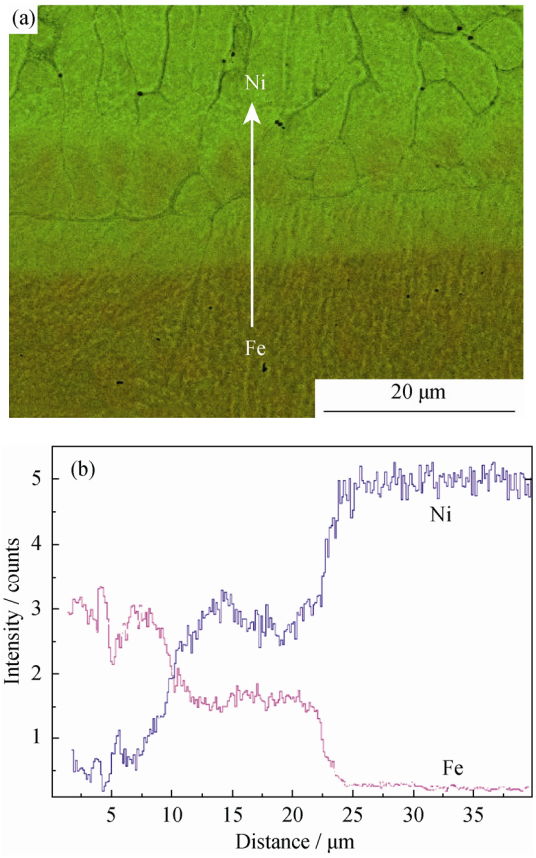

Fig. 10. Mapping of elements Ni and Fe (a) and distribution of Ni and Fe along the transition layer (b).

The presence of steel alloying elements such as nickel, chromium, and copper enhances the steel's corrosion resistance [15]. Moreover, nickel also promotes fracture toughness. These facts suggest that the resulting coating could be used to protect against corrosion.

3.4. Qualitative X-ray analysis

The slits, the angle of incident radiation, and the shooting mode of the diffractometer were selected such that the analyzed area was constant; in particular, its shape was a rectangle with side lengths of approximately 1 and 2 mm. The choice of these shooting conditions enables an analysis of the distribution of phases along the normal to the surface of the sample by a serial shift of 1 mm (Fig. 11).

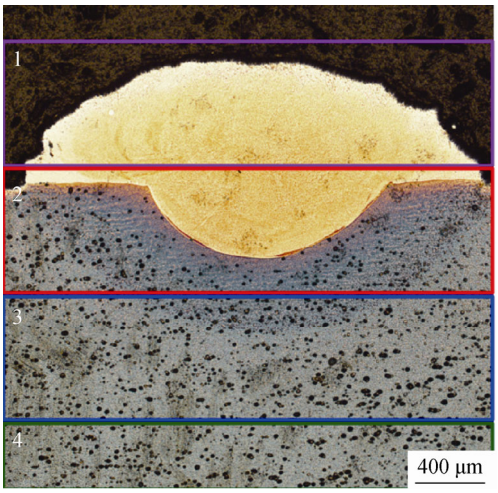

Fig. 11. Schematic of the analyzed sample areas.

Analysis of the diffraction pattern obtained from Region 1 (Fig. 12) leads to a conclusion about the formation of fcc nickel (ICDD PDF-2 01-071-4653) and fcc Fe_3Ni (ICDD PDF-2 01-071-8325), which exhibit lattice parameters of a = 0.3543 nm and a = 0.3573 nm, respectively. Notably, unidentified diffraction peaks were observed at 37.953°, 42.088°, and 45.821°.

The diffraction peaks of the ferrite phase, which is present in the substrate, are observed in the pattern collected at Region 2 (Fig. 13). Notably, the diffraction peaks of fcc Ni and α-Fe have similar values. A graph (Fig. 14) is presented to track the dynamics of the changes in relative intensity of the diffraction peaks. The diffraction patterns of different areas (normalized by the level of background) are presented. The intensity of the diffraction peaks originating from fcc nickel decreases substantially (see Fig. 14), indicating that the content of this phase decreases near the substrate.

A comparative analysis of the relative intensity of fcc Ni and fcc Fe_3Ni peaks (Fig. 14) shows that in the transition

layer, the ratio of the contents of Fe_3Ni to Ni is significantly higher than that in the area of the deposited layer. This fact indicates the intense interaction between nickel and iron.

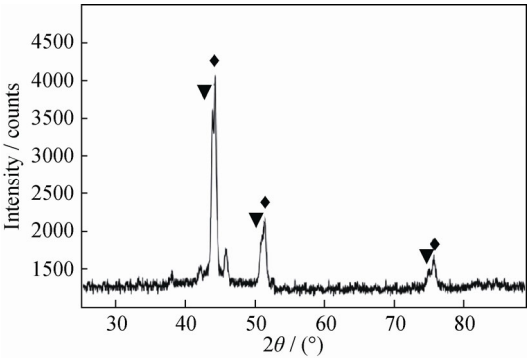

Fig. 12. XRD pattern of the sample obtained from Region 1 in Fig. 11. The diffraction pattern includes peaks of fcc Ni (♦, ICDD PDF-2 01-071-4653) and fcc Fe_3Ni (▼, ICDD PDF-2 01-071-8325).

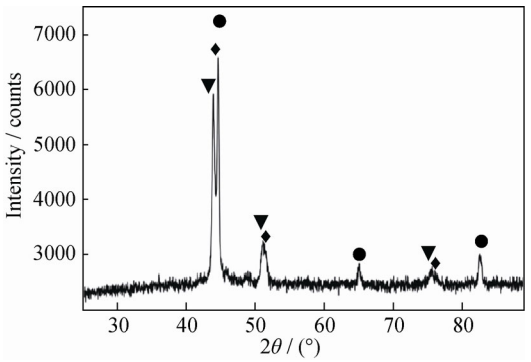

Fig. 13. XRD pattern of the sample obtained from Region 2 in Fig. 11. Diffraction peaks of fcc Ni (♦, ICDD PDF-2 01-071-4653), fcc Fe_3Ni (▼, ICDD PDF-2 01-071-8325), and α-Fe (●, ICDD PDF-2 03-065-4899) are observed in the diffraction pattern.

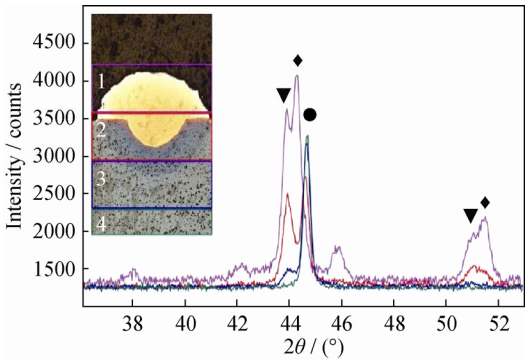

Fig. 14. Diffraction patterns of the sample obtained from different areas. Frame color corresponds to the color line diffractogram obtained in this area. Diffraction peaks of fcc Ni (♦, ICDD PDF-2 01-071-4653), fcc Fe_3Ni (▼, ICDD PDF-2 01-071-8325), and α-Fe (●, ICDD PDF-2 03-065-4899) are observed in the diffraction pattern.

In diffraction Region 3 (Fig. 15), diffraction peaks from fcc nickel are absent and Fe_3Ni peaks exhibit low intensity, indicating a decrease in the content of this phase.

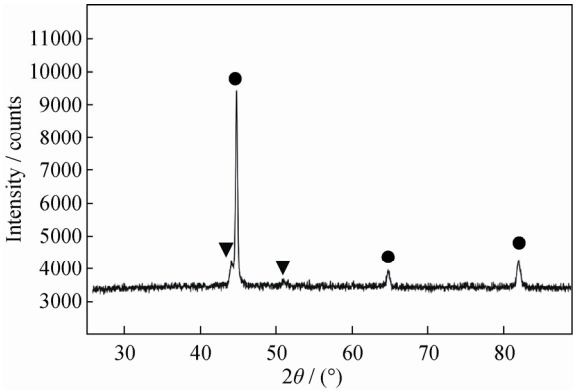

Fig. 15. XRD pattern of the sample obtained from Region 3 in Fig. 11. Diffraction peaks of fcc Fe_3Ni (▼, ICDD PDF-2 01-071-8325) and α-Fe (●, ICDD PDF-2 03-065-4899) are observed.

The diffraction peaks of iron ferrite phase are observed in the diffraction pattern from Region 4 (Fig. 16), which corresponds to the substrate.

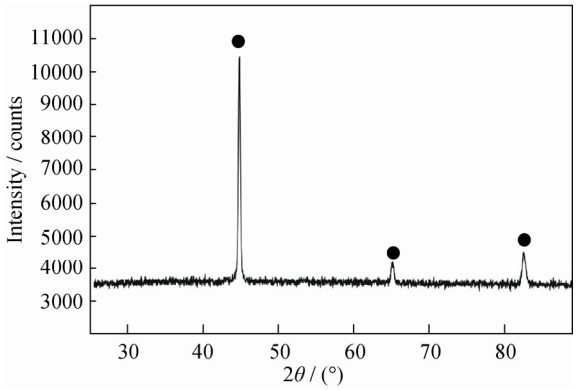

Fig. 16. XRD pattern of the sample obtained from Region 4 in Fig. 11. Diffraction peaks of α-Fe (●, ICDD PDF-2 03-065-4899) are observed.

4. Conclusions

(1) The deposition speed and laser power significantly influence the shape and size of the beads.

(2) The depth of diffusion of nickel into the steel substrate after deposition is less than 20 μm.

(3) The microstructure of the resulting coating is fcc Fe_3Ni.

(4) The size of powder particles directly affects the roughness of the resulting products; no substantial change is detected in the shape of the beads.

(5) The parameters of laser deposition of nickel powder

are recommended for further use in the module 10 R60 CLAD LASER (IPG Photonics); these parameters enable better bead formation and result in a suitable mixing ratio.

Acknowledgements

The work has been done in Kazan National Research Technical University named after A.N. Tupolev under the support of the Ministry of Education and Science of the Russian Federation, state contract No. 14.Z50.31.0023 within the scope of the 220th Enactment and under the state assignment No. 9.3236.2017/PCH.

References

[1] J.C. Ion, *Laser Processing of Engineering Materials: Principles, Procedure, and Industrial Application*, Elsevier, Amsterdam, 2005, p. 556.

[2] W.M. Steen, *Laser Material Processing,* 3rd Ed., Springer, Berlin, 2003, p. 408.

[3] E. Toyserkani, A. Khajepour, and S. Corbin, *Laser Cladding*, CRS Press, Boca Raton, 2005, p. 280.

[4] X.L. Wu, *In situ* formation by laser cladding of a TiC composite coating with a gradient distribution, *Surf. Coat. Technol.*, 115(1999), No. 2-3, p. 111.

[5] F. Moures, E. Cicală, P. Sallamand, D. Grevey, B. Vannes, and S. Ignat, Optimization of refractory coatings realized with cored wire addition using a high-power diode laser, *Surf. Coat. Technol.*, 200(2005), No. 7, p. 2283.

[6] U. de Oliveira, V. Ocelik, and J.T.M. de Hosson, Analysis of coaxial laser cladding processing conditions, *Surf. Coat. Technol.*, 197(2005), No. 2-3, p. 127.

[7] O.G. Devoyno, P. Drozdov, Y.B. Dovoretskiy, M.A. Kardapolova, N.I. Lutsko, and E. Tamanis, Influence of laser cladding parameters on the distribution of elements in the beads of nickel-based Ni–Cr–B–Si alloy, *Latv. J. Phys. Tech. Sci.*, 49(2012), No. 4, p. 61.

[8] A.G. Grigor'yants, I.N. Shiganov, and A.I. Misyurov, *Technological Processes of Laser Processing*, Bauman MSTU Publ., Moscow, 2008, p. 664.

[9] A.G. Grigor'yants, A.N. Safonov, and V.V. Shibaev, *Powder Metallurgy*, Moscow, 1984, No. 9, p. 39.

[10] P.Y. Xia, F. Yan, F.R. Kong, C.M. Wang, J.H. Liu, X.Y. Hu, and S.Y. Pang, Prediction of weld shape for fiber laser keyhole welding based on finite element analysis, *Int. J. Adv. Manuf. Technol.*, 75(2014), No. 1, p. 363.

[11] Z.Q. Chen and X.D. Gao, Detection of weld pool width using infrared imaging during high-power fiber laser welding of type 304 austenitic stainless steel, *Int. J. Adv. Manuf. Technol.*, 74(2014), No. 9, p. 1247.

[12] S.C. Li, G.Y. Chen, C Zhou, X.F. Chen, and Y. Zhou, Plasma inside and outside keyhole during 10 kW level fiber laser welding, *Acta Phys. Sin.*, 63(2014), No. 10, p. 104212.

[13] A.G. Grigoryants, A.I. Misyurov, and R.S. Tretjakov, Analysis of the effect of the parameters of coaxial laser surfacing on the formation of beads, *Tekhnologiya Mashinostroeniya*, 2011, No. 11, p. 19.

[14] C.Y. Kong, P.A. Carroll, P. Brown, and R.J. Scudamore, The effect of average powder particle size on deposition efficiency, deposit height and surface roughness in the direct metal laser deposition process, [in] *Proceedings of the 14th International Conference on Joining of Materials*, Helsingør, Denmark, 2007.

[15] R. Bjorhovde, Development and use of high performance steel, *J. Constr. Steel Res.*, 60(2004), No. 3-5, p. 393.